Derivation of the Small Signal Response and Equivalent Circuit Model for a Separate Absorption and Multiplication Layer Avalanche Photodetector

Daoxin Dai, *Member, IEEE*, Mark J. W. Rodwell, *Fellow, IEEE*, John E. Bowers, *Fellow, IEEE*, Yimin Kang, *Member, IEEE*, and Mike Morse, *Member, IEEE*

***Abstract*—A small signal analysis for a separate-absorption-charge-multiplication (SACM) avalanche photodetector (APD) is presented for the general case when the electrons and the holes have different ionization coefficients and different velocities. The analytic expressions for the impedance and frequency response are given and a simplified equivalent circuit (including an inductance with a series resistance in parallel with a capacitance) for the APD is obtained. The calculation and experimental results show that the impedance of the APD operated at high bias voltages has a maximal value at a certain frequency due to the resonance of the *LC*-circuit, and this is the origin for a peak-enhancement of the frequency response.**

***Index Terms*—Avalanche photodetector (APD), Ge, Si.**

I. Introduction

HIGHLY sensitive photodetectors are desirable for a wide range of applications. One important metric is the gain-bandwidth product (GBP), which is typically in the 80–200 GHz range for III–V avalanche photodetectors (APDs), as is expected for a k value (i.e., the ionization ratio) $\sim$0.4–0.5 [1]. Silicon has a low k-value ($<$0.1), which is desirable for a high GBP, and can be applied to communication applications at 1.3 and 1.55 μm, respectively, when combined with a material with a high absorption coefficient in the infrared, such as InGaAs [2] or Ge [3]–[5]. Kang *et al.* reported CMOS-compatible Ge/Si separate-absorption-charge-multiplication (SACM) APDs with a GBP as high as 340 GHz [3]. Zaoui *et al.* [6], [7] examined higher voltage operation of these diodes and observed a peak enhancement of the frequency response and high gain bandwidth products (840 GHz). Peak enhancement has also been observed for other types of APDs [9]–[11] and is sometimes explained as due to space charge effects. In our previous paper [12], we noted that the impedance for the Ge/Si APD could be fit with an equivalent circuit containing an inductive element and the parameters for the elements in the equivalent circuit were extracted by fitting the measured S_{22} with a genetic algorithm optimization. It was shown that the inductive element plays an important role for the peak enhancement of the frequency response.

Small signal modeling based on fundamental equations (e.g., the Poisson equation and the semiconductor transport equations) is a fundamental and important approach to understand the RF behavior of an APD. Small signal analysis is helpful to make clear the physical mechanism and consequently has been used very widely, e.g., for an RF analysis for impact ionization avalanche transit-time (IMPATT) diodes [13], [14], and for p-n junctions in breakdown [15]. The previous small signal model was developed for IMPATT oscillators and usually with the assumption that the electrons and the holes have equal ionization rates and velocities [15]. In [16], Manasse *et al.*. considered the differences in hole and electron velocities and ionization rates and gave an improved dispersion relationship of a p-n junction avalanche diode, however, for the case with a *single* uniform depletion layer.

In this paper, we present a small signal analysis to calculate the impedance characteristic and the frequency response of an SACM APD, which includes different parameters for the absorption layer and the multiplication layer. Specifically, we consider the general case that the electrons and the holes have different ionization coefficients and different velocities. It is the first derivation of the peak enhancement of the frequency response. Furthermore, we use this analysis to derive the equivalent circuit model for an SACM APD. From the small signal analysis, we obtain analytical expressions for the impedance and the short-circuit frequency response of the APD and compare to experimental results for Ge/Si APDs as an example.

II. Theory

Fig. 1 shows the schematic configuration of an SACM APD. There is thin charge layer between the multiplication layer and the absorption layer, which is doped such that one obtains sufficient gain via a high electric field in the multiplication layer, but the electric field in the absorber is low enough that avalanche gain almost does not occur in the absorption layer (see Fig. 1). The charge layer is usually very thin (100 nm in [3]), so we simplify the APD structure into an avalanche layer and an absorption layer, with uniform electrical fields in each. In the following analysis, we consider the avalanche region and the drift region separately.

Manuscript received September 1, 2009; revised November 7, 2009. This work was supported by the Defense Advanced Research Projects Agency under Contract HR0011-06-3-0009.

D. Dai, M. J. W. Rodwell, and J. E. Bowers are with the Department of Electrical and Computer Engineering, University of California at Santa Barbara, Santa Barbara, CA 93106 USA (e-mail: dxdai@ece.ucsb.edu; rodwell@ece.ucsb.edu; bowers@ece.ucsb.edu).

Y. Kang and M. Morse are with Intel Corporation, Santa Clara, CA 95054 USA (e-mail: yimin.kang@intel.com; mike.morse@intel.com).

Color versions of one or more of the figures in this paper are available online at http://ieeexplore.ieee.org.

Digital Object Identifier 10.1109/JSTQE.2009.2038497

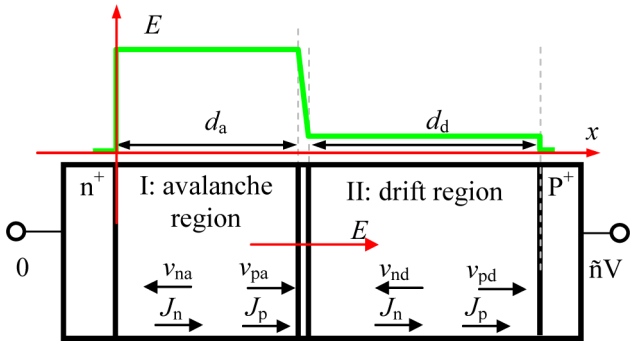

Fig. 1. Structure and electric field distribution for an SACM APD.

A. Avalanche Region

The basic equations for carrier transport in the avalanche region are given as follows:

$$\left.\begin{aligned}\frac{\partial E}{\partial x} &= \frac{q}{\varepsilon_a}(N_D^+ - N_A^- + p - n)\\ J_n &= q|v_{na}|n\\ J_p &= q|v_{pa}|p\end{aligned}\right\}(v_{na}<0, v_{pa}>0)$$

$$\left.\begin{aligned}\frac{\partial n}{\partial t} &= \frac{1}{q}\frac{\partial J_n}{\partial x} + \alpha|v_{na}|n + \beta|v_{pa}|p\\ \frac{\partial p}{\partial t} &= -\frac{1}{q}\frac{\partial J_p}{\partial x} + \alpha|v_{na}|n + \beta|v_{pa}|p\end{aligned}\right\}. \tag{1}$$

Here, we use a small signal model to obtain the solution

$$\begin{cases} E = E_0 + \tilde{E}e^{i\omega t},\\ \alpha(E) \approx \alpha(E_0) + \frac{\partial\alpha}{\partial E}\tilde{E}e^{i\omega t} \equiv \alpha_0 + \alpha'\tilde{E}e^{i\omega t}\\ J_n = J_{n0} + \tilde{J}_n e^{i\omega t}\\ J_p = J_{p0} + \tilde{J}_p e^{i\omega t}\\ n = n_0 + \tilde{n}e^{i\omega t}\\ p = p_0 + \tilde{p}e^{i\omega t}\end{cases} \tag{2}$$

where $\tilde{E}$, $\tilde{J}_n$, and $\tilde{J}_p$ are position-dependent. Substituting (2) into (1), results in the following equations for the ac components:

$$\begin{cases}\frac{\partial\tilde{E}}{\partial x} = \frac{1}{\varepsilon_a}\left(-\frac{\tilde{J}_n}{|v_{na}|} + \frac{\tilde{J}_p}{|v_{pa}|}\right)\\ -\frac{\partial\tilde{J}_n}{\partial x} = \left(\alpha_0 - \frac{i\omega}{|v_{na}|}\right)\tilde{J}_n + c\alpha_0\tilde{J}_p + \bar{J}\alpha'\tilde{E}\\ \frac{\partial\tilde{J}_p}{\partial x} = \alpha_0\tilde{J}_n + \left(c\alpha_0 - \frac{i\omega}{|v_{pa}|}\right)\tilde{J}_p + \bar{J}\alpha'\tilde{E}\end{cases} \tag{3}$$

where $\bar{J} \equiv J_{n0} + cJ_{p0}$ and $c = \beta/\alpha$. Equation (3) has the following solutions:

$$\begin{cases}\tilde{E} = C_1 e^{-i\gamma_1 x} + C_2 e^{-i\gamma_2 x} + C_3\\ \tilde{J}_n = A_1C_1 e^{-i\gamma_1 x} + A_2C_2 e^{-i\gamma_2 x} + A_3C_3\\ \tilde{J}_p = B_1C_1 e^{-i\gamma_1 x} + B_2C_2 e^{-i\gamma_2 x} + B_3C_3\end{cases} \tag{4}$$

where

$$\begin{cases} A_1 = \frac{-i\varepsilon_a(\omega|v_{na}|/|v_{pa}| - \gamma_1|v_{na}|)}{1+|v_{na}|/|v_{pa}|}\\ B_1 = \frac{-i\varepsilon_a(\omega+\gamma_1|v_{na}|)}{1+|v_{na}|/|v_{pa}|}\end{cases}$$

$$\begin{cases} A_2 = \frac{-i\varepsilon_a(\omega|v_{na}|/|v_{pa}| - \gamma_2|v_{na}|)}{1+|v_{na}|/|v_{pa}|}\\ B_2 = \frac{-i\varepsilon_a(\omega+|v_{na}|\gamma_2)}{1+|v_{na}|/|v_{pa}|}\\ A_3 = \frac{-|v_{na}|\alpha'\bar{J}}{\alpha_0(|v_{na}|+c|v_{pa}|)-i\omega}\\ B_3 = \frac{-|v_{pa}|\alpha'\bar{J}}{\alpha_0(|v_{na}|+c|v_{pa}|)-i\omega}\end{cases}$$

and the eigenvalues γ_1 and γ_2 are given by

$$\gamma_{1,2} = \frac{1}{2}(-b_0 \pm \sqrt{b_0^2 - 4c_0}) \tag{5}$$

in which

$$\begin{cases} b_0 = -\left[i(c-1)\alpha_0 + \omega\left(\frac{1}{|v_{pa}|} - \frac{1}{|v_{na}|}\right)\right]\\ c_0 = \frac{1}{\varepsilon_a}\left(\frac{1}{|v_{na}|}+\frac{1}{|v_{pa}|}\right)\alpha'\bar{J} - \frac{1}{|v_{na}||v_{pa}|}\omega^2\\ \qquad -i\left(\frac{1}{|v_{pa}|}+\frac{1}{|v_{na}|}c\right)\omega\alpha_0.\end{cases}$$

The total ac current is given by $J = \tilde{J}_n + \tilde{J}_p + \tilde{J}_d$, where the displacement current $\tilde{J}_d = i\omega\varepsilon_a\tilde{E}$. Then we have

$$C_3 = \frac{J}{a_3} \tag{6}$$

where

$$a_3 = i\omega\varepsilon_a - \frac{|v_{pa}|+|v_{na}|}{\alpha_0(|v_{na}|+c|v_{pa}|)-i\omega}\alpha'\bar{J}.$$

The constants C_1 and C_2 will be determined according to the boundary conditions given in the following (see Section II-C).

B. Drift Region

Now let us consider the drift region where the basic equations are given as follows:

$$\left.\begin{aligned}\frac{\partial\tilde{E}}{\partial x} &= \frac{1}{\varepsilon_d}\left(\frac{\tilde{J}_p}{|v_{pd}|} - \frac{\tilde{J}_n}{|v_{nd}|}\right)\\ \frac{\partial\tilde{J}_n}{\partial x} &= i\omega\frac{\tilde{J}_n}{|v_{nd}|} - q\tilde{g}\\ \frac{\partial\tilde{J}_p}{\partial x} &= -i\omega\frac{\tilde{J}_p}{|v_{pd}|} + q\tilde{g}\end{aligned}\right\} \tag{7}$$

where $\tilde{g}$ is the photo-carrier generation rate. The solutions are given as follows:

$$\begin{cases}\tilde{E} = C_1' e^{-i\gamma_1' x} + C_2' e^{-i\gamma_2' x} + C_3'\\ \tilde{J}_n = A_1'C_1' e^{-i\gamma_1' x} + A_2'C_2' e^{-i\gamma_2' x} + A_3'C_3'\\ \tilde{J}_p = B_1'C_1' e^{-i\gamma_1' x} + B_2'C_2' e^{-i\gamma_2' x} + B_3'C_3'\end{cases} \tag{8}$$

where

$$\begin{cases} A_1' = B_2' = -i\omega\varepsilon_d \\ A_2' = B_1' = 0 \end{cases}, \quad \begin{cases} A_3'C_3' = q\tilde{g}\dfrac{|v_{nd}|}{i\omega} \\ B_3'C_3' = q\tilde{g}\dfrac{|v_{pd}|}{i\omega} \end{cases}, \quad \text{and}$$

$$\begin{cases} \gamma_1' = -\dfrac{\omega}{|v_{nd}|} \\ \gamma_2' = \dfrac{\omega}{|v_{pd}|} \end{cases}.$$

From $J = \tilde{J}_n + \tilde{J}_p + i\omega\varepsilon_d\tilde{E}$, we have

$$C_3' = \frac{J}{a_{3'} + b_{3'}} \tag{9}$$

where $a_{3\prime} = i\omega\varepsilon_d$ and $b_{3\prime} = q\tilde{g}(|v_{nd}| + |v_{pd}|)/(\omega^2\varepsilon_d)$. The constants C_1' and C_2' will be determined according to the following boundary conditions.

C. Boundary Conditions

At the left side (n-contact) and the right side (p-contact), we have

$$\tilde{J}_n|_{x=d_d+d_a} = \tilde{J}_{ns}$$
$$\tilde{J}_p|_{x=0} = \tilde{J}_{ps}$$

where $\tilde{J}_{ns}$ and $\tilde{J}_{ps}$ are the saturation currents of the electrons and holes, respectively. From these two equations for boundary conditions, we have

$$C_1' = \frac{\tilde{J}_{ns} - q\tilde{g}|v_{nd}|/(i\omega)}{A_1' e_{1da'}} \tag{10a}$$

$$B_1C_1 + B_2C_2 = \tilde{J}_{ps} - B_3C_3 \tag{10b}$$

where $e_{1da'} = exp[-i\gamma_1'(d_a + d_d)]$.

At the interface between the avalanche region and the drift region, the electron and hole currents should be continuous, i.e.,

$$\tilde{J}_n|_{x=d_a^+} = \tilde{J}_n|_{x=d_a^-} \quad \text{and} \quad \tilde{J}_p|_{x=d_a^+} = \tilde{J}_p|_{x=d_a^-}$$

and consequently we have

$$A_1C_1e_{1a} + A_2C_2e_{2a} = A_1'C_1'e_{1a'} + A_3'C_3' - A_3C_3 \tag{11a}$$

$$B_1C_1e_{1a} + B_2C_2e_{2a} + B_3C_3 = B_2'C_2'e_{2a'} + B_3'C_3' \tag{11b}$$

where

$$\begin{cases} e_{1a} = e^{-i\gamma_1 d_a} \\ e_{2a} = e^{-i\gamma_2 d_a} \end{cases} \quad \text{and} \quad \begin{cases} e_{1a'} = e^{-i\gamma_1' d_a} \\ e_{2a'} = e^{-i\gamma_2' d_a} \end{cases}.$$

For the avalanche region ($0 < x < d_a$), the voltage is given by

$$\tilde{V}_1 = \int_0^{d_a} \tilde{E}\,dx = i\frac{C_1}{\gamma_1}(e_{1a} - 1) + i\frac{C_2}{\gamma_2}(e_{2a} - 1) + C_3 d_a.$$

For the drift region ($d_a < x < d_a + d_d$), the voltage is given by

$$\begin{aligned} \tilde{V}_2 &= \int_{d_a}^{d_d+d_a} \tilde{E}\,dx \\ &= i\frac{C_1'}{\gamma_1'}(e_{1da'} - e_{1a'}) + i\frac{C_2'}{\gamma_2'}(e_{2da'} - e_{2a'}) + C_3'd_d \end{aligned}$$

where

$$\begin{cases} e_{1da'} = \exp[-i\gamma_1'(d_d + d_a)] \\ e_{2da'} = \exp[-i\gamma_2'(d_d + d_a)] \end{cases}.$$

The total voltage $\tilde{V}$ is then given by

$$\tilde{V} = \tilde{V}_1 + \tilde{V}_2. \tag{12}$$

From (10b) and (11a), we have the solutions for C_1 and C_2 as given by

$$C_1 = c_{11} + c_{12}J \tag{13a}$$

$$C_2 = c_{21} + c_{22}J \tag{13b}$$

where

$$\begin{cases} c_{11} = (A_2e_{2a}b_{11} - B_2b_{21})/|A| \\ c_{12} = (A_2e_{2a}b_{12} - B_2b_{22})/|A| \\ c_{21} = (B_1b_{21} - A_1e_{1a}b_{11})/|A| \\ c_{22} = (B_1b_{22} - A_1e_{1a}b_{12})/|A| \end{cases}$$

$$|A| = \begin{vmatrix} B_1 & B_2 \\ A_1e_{1a} & A_2e_{2a} \end{vmatrix} \text{ and } \begin{cases} b_{11} = \tilde{J}_{ps} \\ b_{12} = -B_3 \rightleftarrows /a_3 \\ b_{21} = A_1'C_1'e_{1a'} + A_3'C_3' \\ b_{22} = -A_3/a_3 \end{cases}$$

From (11b), we have

$$C_2' = c_{21'} + c_{22'}J \tag{14}$$

where

$$\begin{cases} c_{21'} = \dfrac{c_{11}B_1e_{1a} + c_{21}B_2e_{2a} - B_3'C_3'}{B_2'e_{2a'}} \\ c_{22'} = \dfrac{c_{12}B_1e_{1a} + c_{22}B_2e_{2a} + B_3/a_3}{B_2'e_{2a'}} \end{cases}.$$

Now, we obtain the expressions for all the constants $C_1, C_2, C_3, C_1', C_2'$, and C_3' [see (13a), (13b), (6), (10a), (14), and (9)] for the solutions (4) and (8). Inserting these results into (12), we have

$$\begin{aligned} \tilde{V} = J\Bigg(& i\frac{e_{1a}-1}{\gamma_1}c_{12} + i\frac{e_{2a}-1}{\gamma_2}c_{22} \\ & + \frac{d_a}{a_3} + i\frac{e_{2da'} - e_{2a'}}{\gamma_2'}c_{22'} + \frac{d_d}{a_{3'}}\Bigg) \\ & + i\frac{e_{1a}-1}{\gamma_1}c_{11} + i\frac{e_{2a}-1}{\gamma_2}c_{21} + i\frac{C_1'}{\gamma_1'}(e_{1da'} - e_{1a'}) \\ & + i\frac{e_{2da'} - e_{2a'}}{\gamma_2'}c_{21'} + d_d b_{3'}. \end{aligned} \tag{15}$$

Finally, we have the following analytical expression for the ac current (16), as shown at the bottom of the next page.

From the way impedance is measured and from its definition, we set $\tilde{g} = 0$ when calculating the impedance. Consequently, we have

$$c_{11} \approx 0,\ c_{21} \approx 0,\ C_1' = 0,\ c_{21'} \approx 0,\ b_{3'} = 0.$$

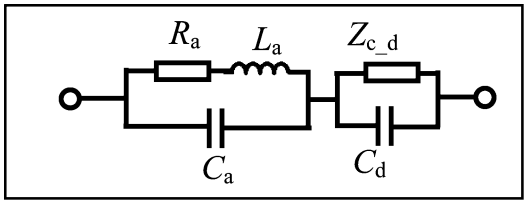

Fig. 2. Simplified equivalent circuit for the APD impedance Z given by (17).

Thus, the impedance is then given by

$$Z = \frac{\tilde{V}}{JS} = \frac{1}{S}\left(i\frac{e_{1a}-1}{\gamma_1}c_{12} + i\frac{e_{2a}-1}{\gamma_2}c_{22} + \frac{d_a}{a_3} + i\frac{e_{2da'}-e_{2a'}}{\gamma_2'}c_{22'} + \frac{d_d}{a_{3'}}\right) \tag{17}$$

where S is the APD area. With some more derivation (as shown in the Appendix), we obtain a simplified equivalent circuit for the APD impedance given by (17), as shown in Fig. 2. In this equivalent circuit, an inductance, a resistance and a capacitance are included for the avalanche region. The inductance and the series resistance can be explained as follows. When applying an ac bias voltage on the avalanche region, both the ionization coefficient and the carrier density are modulated. The time variation rate of the carrier density $\partial n/\partial t$ (as well as $\partial p/\partial t$) is not only related with the ac electric field but also the carrier density itself. The interaction between the ac electric field and the ac carrier density introduces an inductance with a series resistance. Particularly, the inductance is due to the phase delay between the ac-current and the electric field (i.e., the ac voltage). In the drift region, there is no avalanche process and consequently no inductance effect. The impedance Z_{c_d} is the part corresponding to the conduction current. The parameters for the elements are given by

$$R_a = -\alpha_0 \frac{|v_{na}| + c|v_{pa}|}{|v_{na}| + |v_{pa}|}\frac{d_a}{\alpha' \bar{J}S}$$

$$L_a = \frac{1}{|v_{na}| + |v_{pa}|}\frac{d_a}{\alpha' \bar{J}S}$$

$$C_a = \frac{\varepsilon_a S}{d_a}$$

$$C_d = \frac{\varepsilon_d S}{d_d}.$$

$$Z_{c\_d} = -\frac{1}{i\omega\varepsilon_d S/d_d} + \frac{d_d^2}{S}\frac{1}{i\omega\varepsilon_d^2}\frac{1}{|v_{pd}|}\frac{1}{e_{2da'}-e_{2a'}}\frac{1}{c_{22'}}.$$

From these formulae, one sees that the inductance L_a and the series resistance R_a are inversely proportional to the direct current $\bar{J}S$ and the differential α'. Usually, the inductance ranges from sub-nH to several nH and the series resistance R_a ranges from hundreds of Ohm to several Ohm, which depends on the value to the direct current $\bar{J}S$ and the differential α'.

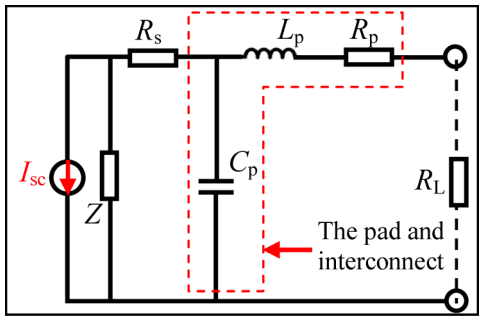

Fig. 3. APD equivalent circuit including parasitic effects.

This simplified equivalent circuit is helpful for understanding the behavior of the APD impedance and frequency responses and to determine matching circuits for the diode. However, for greater accuracy, we use the APD impedance Z given by (17) in the rest of the calculations, and compare the two calculations in later figures.

The short-circuit frequency response I_{sc} of the APD is given by setting $\tilde{V} = 0$ in (16). In order to include the parasitic effects of series resistance (R_p), transmission line inductance (L_p) and pad capacitance (C_p), we use an equivalent circuit as shown in Fig. 3, where R_s is the series resistance. In this equivalent circuit, the current source I_{sc} is given by the response of the APD in the short-circuit case and the impedance Z is given (17).

From Fig. 3, one sees that the current flowing through the load resistance R_L is given by

$$I_L = I_{sc}\kappa \tag{18}$$

where

$$\kappa = \frac{Z}{Z + R_s + 1/(i\omega C_p + 1/(R_L + R_p + i\omega L_p))} \times \frac{1/(i\omega C_p)}{1/(i\omega C_p) + (R_L + R_p + i\omega L_p)}. \tag{19}$$

III. Results and Discussion

Here we compare these calculations to measurements on normal-incidence illuminated SACM Ge/Si APDs. Fig. 4(a) shows the cross section of the APD [3]. Fig. 4(b) shows the top view of the fabricated APD. The thicknesses and the doping concentrations for all layers are shown in Fig. 4(c). A silicon-nitride film was deposited and serves as an antireflection coating in the 1310 nm window to improve the quantum efficiency.

From the measured I–V curves, the dc current is on the order of mA. Even though dc current density for the electrons (J_{n0}) and for the holes (J_{p0}) are x-dependent, in order to have a simplified model we use the averaged current density and assume $J_{n0} = J_{p0}$ in the calculation below. From the Silvaco simulation for the

$$J = \frac{\tilde{V} - (i((e_{1a}-1)/\gamma_1)c_{11} + i((e_{2a}-1)/\gamma_2)c_{21} + i(C_1'/\gamma_1')(e_{1da'}-e_{1a'}) + i((e_{2da'}-e_{2a'})/\gamma_2'))\,(c_{21'} + d_d b_{3'})}{i((e_{1a}-1)/\gamma_1)c_{12} + i((e_{2a}-1)/\gamma_2)c_{22} + (d_a/a_3) + i((e_{2da'}-e_{2a'})/\gamma_2'))c_{22'} + (d_d/a_{3'})} \tag{16}$$

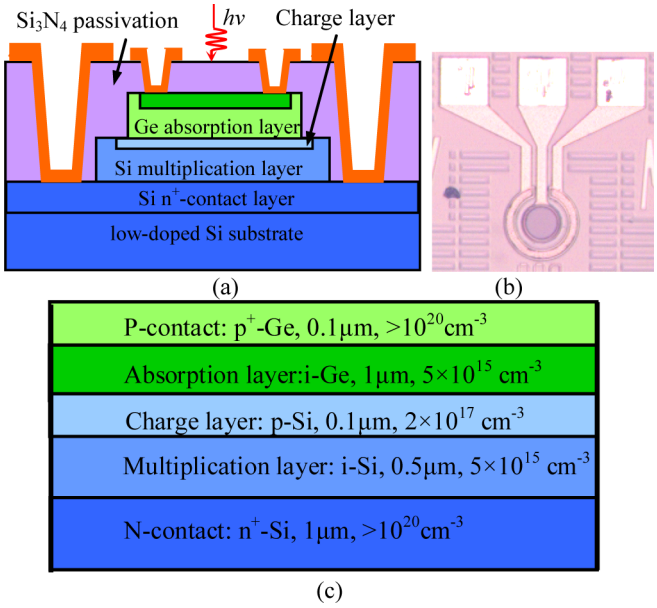

Fig. 4. (a) Schematic configuration of the Ge/Si SACM APD device; (b) top view of the fabricated SCAM Ge/Si APD; (c) parameters (the doping concentrations and the thicknesses) for the layers.

TABLE I
AVALANCHE COEFFICIENTS FOR SI AND GE

material	Si		Ge	
	Electrons	Holes	Electrons	Holes
A_0 (m^{-1})	7.030×10^7	1.580×10^8	1.55×10^7	1.0×10^8
B_0 (V/m)	1.231×10^8	2.036×10^8	1.56×10^8	1.28×10^8
v (cm/s)	10×10^6	7.0×10^6	7×10^6	6.2×10^6

dc electric field distribution shown in [7], one sees that electric field strength is around 400 kV/cm in the avalanche region at a high reverse bias voltage. Therefore, here we give an analysis for the performance of the APD operated at around $E = 400$ kV/cm. The ionization coefficients for the electrons and the holes are given by: $\alpha, \beta = A_0 \exp(-B_0/E)$, where the coefficients are given in Table I [17]. In Table I, the electron/hole saturation velocities of Si and Ge are also given [7]. In our calculation, we use the saturation velocities. This is true at high bias voltage which is the case considered in this paper.

Fig. 5(a) shows the real part and the imaginary part of the impedance Z, which shows a strong dependence on the electric-field strength. When the electric field is relatively weak (e.g., $E = 385$ kV/cm), the real part is positive and decreases monotonically with frequency, while the imaginary part is negative and has a minimal value at a certain frequency. This is essentially a parallel-connected resistance–capacitance (RC) circuit, as is seen for a PIN detector. When the electric field is stronger, the impedance becomes very different [$E > 400$ kV/cm curves in Fig. 5(a)]. The real part Z_r of the impedance has a peak at a certain frequency f_r and the imaginary part Z_i of the impedance has a transition from a positive to a negative value at almost the same position f_r. This indicates that there is an inductance and a capacitance in the equivalent circuit. When $f < f_r$, the imaginary part Z_i is positive since the inductance plays an important

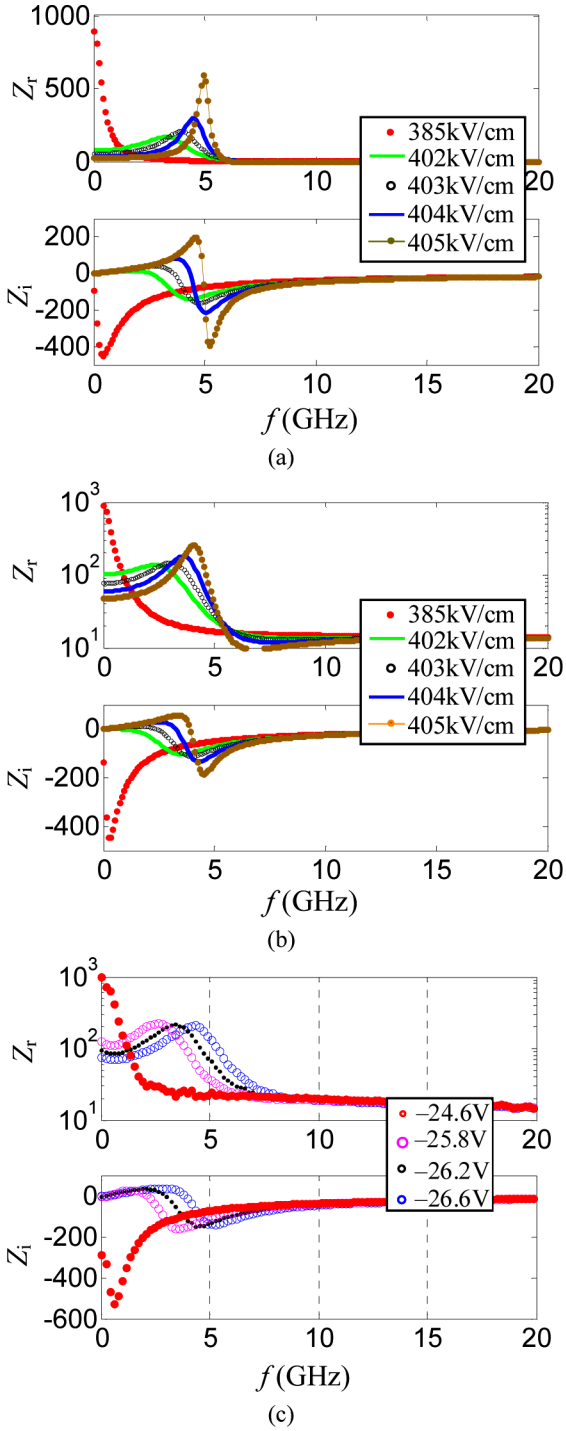

Fig. 5. Real part and the imaginary part of the impedance for: (a) APD without parasitic effects; (b) APD with parasitic effects (R_p, C_p, and L_p); (c) measurement results.

role. When $f > f_r$, the capacitance plays an important role and consequently the imaginary part Z_i becomes negative. The inductance effect is because the impact ionization in the avalanche region introduces a phase delay between the ac current and the electric field (i.e., the ac voltage).

In order to compare the measured impedance of the APD with the GSG pads, we calculate the total APD impedance with the parasitic effects, including the inductance L_p, the capacitance

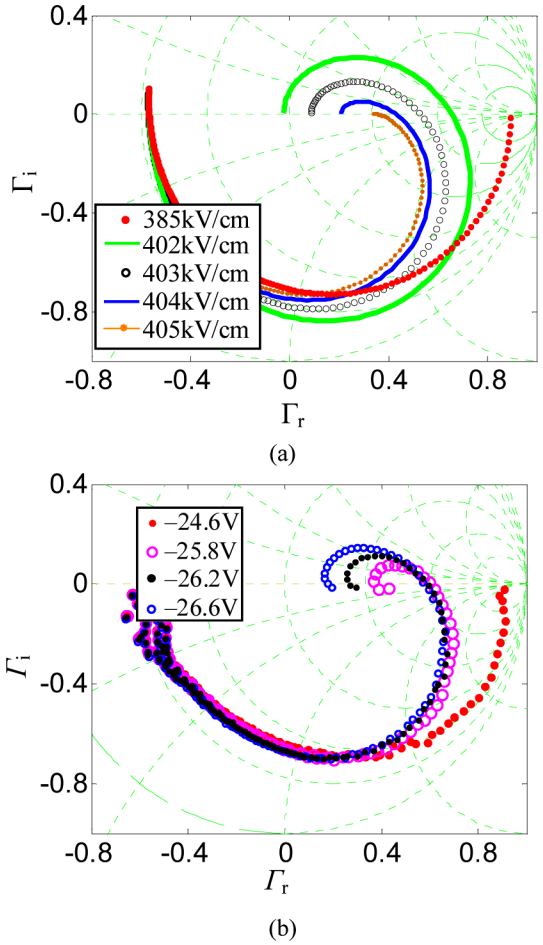

Fig. 6. (a) Calculated Smith chart (the frequency ranges from 45 MHz to 30 GHz); (b) measured Smith chart.

C_p, and the resistance R_p (see Fig. 3). The values for the elements are: $L_p = 0.082$ nH, $C_p = 0.193$ pF, and $R_p = 6.65\ \Omega$ and $R_s = 16.76\ \Omega$, which are estimated from the experimental measurements. The calculated impedance with the parasitic effects is shown in Fig. 5(b). When parasitic effects are included, the total impedance is similar to that shown in Fig. 5(a). In Fig. 5(c), we present the real part Z_r and the imaginary part Z_i of the measured impedance for the APD with $D = 80\ \mu$m when the bias voltage varies from -24.6 to -26.6 V. The impedance was obtained by measuring the microwave reflection parameter S_{22} as the bias voltage is varied by using an Agilent E8364 A network analyzer. From Fig. 5(b) and (c), one sees the calculated results are very close to the measurement results.

In Fig. 6(a) and (b), we also show the calculated and the measured Smith charts. One sees they agree well with each other. The difference between them might be because our model does not include the traps in Ge layer and the interdiffusion layer between the Si and Ge layer. When the bias voltage (or the electric field) is low, the entire curve is below the line $\Gamma_i = 0$ (which corresponds to a resistor and capacitor in parallel, representing the diode capacitance and diode resistance). For a higher bias voltage, one has $\Gamma_i > 0$ in a certain frequency range. The phenomenon becomes stronger when the bias voltage increases further.

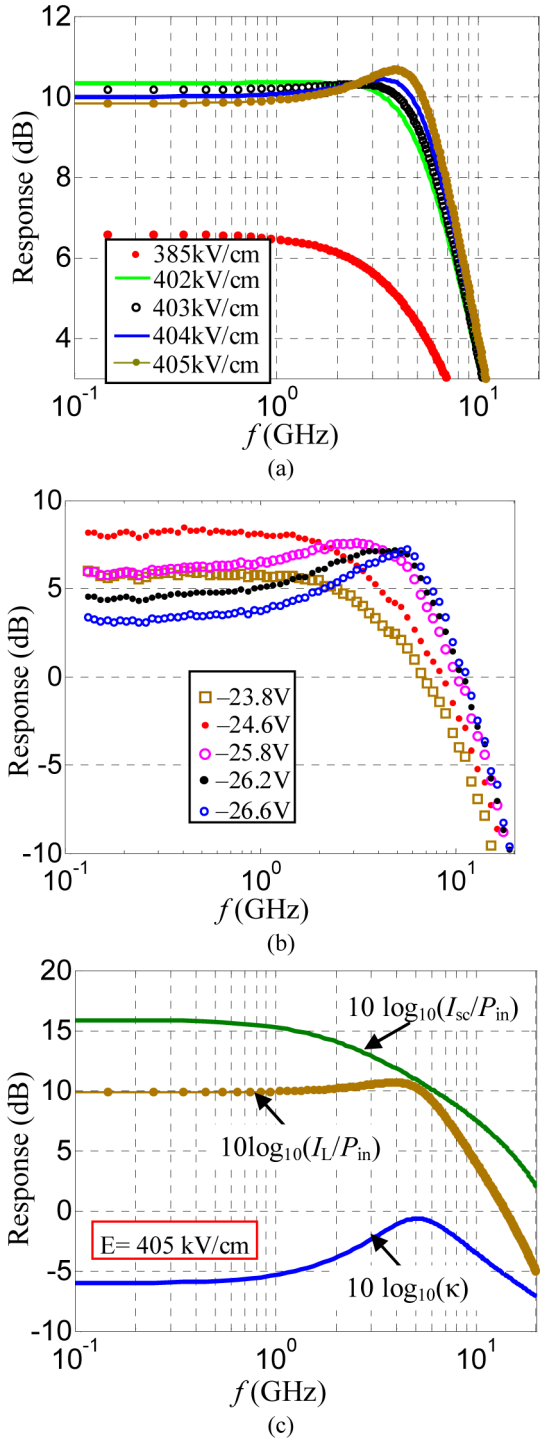

Fig. 7. (a) Calculated frequency responses at different electric field strengths; (b) measured frequency responses at different bias voltages; (c) response when $E = 405$ kV/cm: the top curve is for the short-circuit frequency response (given by $10\log_{10}(I_{\rm sc}/P_{\rm in})$); the bottom curve is the response for κ, which is given by (19); the middle curve is the frequency response of the current flowing through the load resistance given by $10\log_{10}(I_L/P_{\rm in}) = 10\log_{10}(\kappa I_{\rm sc}/P_{\rm in})$.

Fig. 7(a) shows the calculated frequency responses at different electric field strengths. From this figure, one sees that, when the electric field strength increases, the dc gain increases because of more impact ionization [as can be seen in the responses in the low-frequency range shown in Fig. 7(a)]. When the electric field strength is higher (e.g., $E > 402$ kV/cm here), the

response at low frequency decreases while there is an enhancement in the high frequency range. The enhancement becomes greater as the electric field strength increases. This behavior is also observed in our measurement of APDs. Fig. 7(b) shows the measured frequency responses at different bias voltages (ranging from -23.8 to -26.6V). In order to show the origin of the peak enhancement, in Fig. 7(c) we show more details for the frequency response in the case $E = 405$ kV/cm as an example.

In Fig. 7(c), the top curve is for the short-circuit frequency response of APD, which is given by $10\log_{10}(I_{\rm sc}/P_{\rm in})$. The bottom one is the response for κ, which is given by (19), and consequently the parasitic effect is included. The dotted one is the frequency response of the current flowing through the load resistance, which is given by $10\log(I_L/P_{\rm in}) = 10\log_{10}(\kappa I_{\rm sc}/P_{\rm in})$. From Fig. 7(c), one sees the peak-enhancement of the response $10\log_{10}(I_L/P_{\rm in})$ is corresponding to the peak of the coefficient κ. As we see in Fig. 5, the impedance of the APD (without the parasitic effects) has a maximal value, which results in the peak of the coefficient κ. Such a peak enhancement of frequency response will enhance the 3-dB bandwidth when the APD operates at high bias voltage. Consequently it is beneficial to achieve high GBP as shown in the previous paper [7].

IV. Conclusion

In this paper, we have presented a small signal analysis for an SACM APD and obtained analytical expressions for the impedance and the short-circuit frequency response for the APD. It is the first time the peak enhancement of the frequency response has been presented using small-signal modeling. We have also established an equivalent circuit (including the parasitic effects) for the APD. The theoretical prediction agrees well with the experimental results. From the calculation results, it has been shown that the impedance of the APD will have a maximal value at a certain frequency when the bias voltage is high. This is the origin of a peak-enhancement of the response at a high frequency.

Appendix

Here, we obtain the equivalent circuit for the APD impedance Z [given by (17)]. The current density includes two components: the conduction current density and the displacement current density.

1) In the avalanche region, the impedance is given by

$$Z_a = \frac{\tilde{V}_1}{J_{c\_a}S + J_{d\_a}S} = \frac{1}{(1/Z_{c\_a}) + (1/Z_{c\_d})} \tag{A1}$$

where J_{c_a} and J_{d_a} are the conduction current density and the displacement current density, respectively, and the impedances $Z_{c\_a} = \tilde{V}_1/(J_{c\_a}S)$ and $Z_{d\_a} = \tilde{V}_1/(J_{d\_a}S)$. The conduction current density J_{c_a} is given by

$$J_{c\_a} = \frac{1}{d_a}\int_0^{d_a} (\tilde{J}_n + \tilde{J}_p)dx. \tag{A2}$$

Thus, the impedance is then given by, (A3), as shown at the bottom of this page.

Since γ_1 and γ_2 are usually very large (especially at the high frequency), we have

$$i\frac{C_1}{\gamma_1}(e_{1a} - 1) + i\frac{C_2}{\gamma_2}(e_{2a} - 1) + C_3 d_a \approx C_3 d_a \tag{A4}$$

and

$$Z_{c\_a} \equiv R_a + i\omega L_a \tag{A5}$$

where

$$R_a = -\alpha_0 \frac{|v_{na}| + c|v_{pa}|}{|v_{na}| + |v_{pa}|}\frac{d_a}{\alpha'\bar{J}S} \tag{A6a}$$

$$L_a = \frac{1}{|v_{na}| + |v_{pa}|}\frac{d_a}{\alpha'\bar{J}S}. \tag{A6b}$$

The impedance Z_{d_a} is given as follows:

$$Z_{d\_a} = \frac{i\omega\varepsilon_a S}{d_a} \equiv i\omega C_a \tag{A7}$$

where

$$C_a = \frac{\varepsilon_a S}{d_a}. \tag{A8}$$

2) In the drift region, similarly we have

$$Z_d = \frac{\tilde{V}_2}{J_{c\_d}S + J_{d\_d}S} = \frac{1}{1/Z_{c\_d} + 1/Z_{d\_d}} \tag{A9}$$

where $Z_{c\_d} = \tilde{V}_2/(J_{c\_d}S)$ and $Z_{d\_d} = \tilde{V}_2/(J_{d\_d}S)$.

The conduction current density J_{c_d} is given by

$$J_{c\_d} = \frac{1}{d_d}\int_{d_a}^{d_a+d_d} (\tilde{J}_n + \tilde{J}_p)dx \tag{A10}$$

Consequently, we have (A11), as shown at the bottom of this page.

Since $\tilde{g} = 0$ (for calculating the impedance), one has

$$c_{11} \approx 0, c_{21} \approx 0, C_1' = 0, c_{21'} \approx 0, b_{3'} = 0.$$

$$Z_{c\_a} = \frac{d_a/S}{i\omega\varepsilon_a C_3 d_a - (|v_{na}| + |v_{pa}|)\alpha'\bar{J}C_3 d_a/\alpha_0(|v_{na}| + c|v_{pa}|) - i\omega/(i(C_1/\gamma_1)(e_{1a} - 1) + i(C_2/\gamma_2)(e_{2a} - 1) + C_3 d_a) - i\omega\varepsilon_a} \tag{A3}$$

$$Z_{c\_d} = \frac{d_d/S}{(i\omega\varepsilon_d C_3' d_d + ((|v_{nd}| + |v_{pd}|)/i\omega)q\tilde{g}d_d/i(C_1'/\gamma_1')(e_{1da'} - e_{1a'}) + i(C_2'/\gamma_2')(e_{2da'} - e_{2a'}) + C_3' d_d) - i\omega\varepsilon_d} \tag{A11}$$

Consequently (A11) is rewritten as

$$Z_{c\_d} = \frac{d_d}{i\omega\varepsilon_d S}\left(\frac{d_d}{|v_{pd}|\varepsilon_d}\frac{1}{e_{2da'}-e_{2a'}}\frac{1}{c_{22'}}-1\right). \quad \text{(A12)}$$

The impedance Z_{d_d} is given as follows:

$$Z_{d\_d} = \frac{j\omega\varepsilon_d S}{d_d} \equiv j\omega C_d \quad \text{(A13)}$$

where

$$C_d = \frac{\varepsilon_d S}{d_d}. \quad \text{(A14)}$$

REFERENCES

[1] J. C. Campbell, W. T. Tsang, G. J. Qua, and B. C. Johnson, "High-speed InP /InGaAsP /InGaAs avalanche photodiodes grown by chemical beam epitaxy," *IEEE J. Quantum Elecron.*, vol. 24, no. 3, pp. 496–500, Mar. 1988.

[2] A. R. Hawkins, W. Wu, P. Abraham, K. Streubel, and J. E. Bowers, "High gain-bandwidth-product silicon heterointerface photodetector," *Appl. Phys. Lett.*, vol. 70, no. 3, pp. 303–305, 1996.

[3] Y. Kang, H.-D. Liu, M. Morse, M. J. Paniccia, M. Zadka, S. Litski, G. Sarid, A. Pauchard, Y.-H. Kuo, H.-W. Chen, W. S. Zaoui, J. E. Bowers, A. Beling, D. C. McIntosh, X. Zheng, and J. C. Campbell, "Monolithic Ge/Si avalanche photodiodes with 340G Hz gain-bandwidth product," *Nat. Photon.*, vol. 3, no. 1, pp. 59–63, 2009.

[4] S. J. Koester, J. D. Schaub, G. Dehlinger, and J. O. Chu, "Germanium-on-SOI infrared detectors for integrated photonic applications," *IEEE J. Sel. Topics Quantum Electron.*, vol. 12, no. 6, pp. 1489–1502, Nov./Dec. 2006.

[5] S. J. Koester, C. L. Schow, L. Schares, G. Dehlinger, J. D. Schaub, F. E. Doany, and R. A. John, "Ge-on-SOI-detector/Si-CMOS-amplifier receivers for high-performance optical-communication applications," *J. Lightw. Technol.*, vol. 25, no. 1, pp. 46–57, Jan. 2007.

[6] W. S. Zaoui, H.-W. Chen, J. E. Bowers, Y. Kang, M. Morse, M. J. Paniccia, A. Pauchard, and J. Campbell, "Origin of the gain-bandwidth-product enhancement in separate-absorption-charge-multiplication Ge/Si avalanche photodiodes," in *Proc. Opt. Fiber Commun. (OFC)*, San Diego, CA, Mar. 2009, pp. 1–3.

[7] W. S. Zaoui, H.-W. Chen, J. E. Bowers, Y. Kang, M. Morse, M. J. Paniccia, A. Pauchard, and J. C. Campbell, "Frequency response and bandwidth enhancement in Ge/Si avalanche photodiodes with over 840 GHz gain-bandwidth-product," *Opt. Exp.*, vol. 17, no. 15, pp. 12641–12649, 2009.

[8] G. Wang, T. Tokumitsu, I. Hanawa, K. Sato, and M. Kobayashi, "Analysis of high speed p-i-n photodiodes s-parameters by a novel small-signal equivalent circuit model," *IEEE Microw. Wireless Compon. Lett.*, vol. 12, no. 10, pp. 378–380, Oct. 2002.

[9] J.-W. Shi, Y.-S. Wu, Z.-R. Li, and P.-S. Chen, "Impact-ionization-induced bandwidth enhancement of a Si-SiGe-based avalanche photodiode operating at a wavelength of 830 nm with a gain-bandwidth product of 428 GHz," *IEEE Photon. Technol. Lett.*, vol. 19, no. 7, pp. 474–476, Apr. 2007.

[10] M.-J. Lee, H.-S. Kang, and W.-Y. Choi, "Equivalent circuit model for Si avalanche photodetectors fabricated in standard CMOS process," *IEEE Electron Device Lett.*, vol. 29, no. 10, pp. 1115–1117, Oct. 2008.

[11] G. Kim, I. G. Kim, J. H. Baek, and O. K. Kwon, "Enhanced frequency response associated with negative photoconductance in an InGaAs/InAlAs avalanche photodetector," *Appl. Phys. Lett.*, vol. 83, no. 6, pp. 1249–1251, 2003.

[12] D. Dai, H.-W. Chen, J. E. Bowers, Y. Kang, M. Morse, and M. J. Paniccia, "Resonant normal-incidence separate-absorption-charge-multiplication Ge/Si avalanche photodiodes," *Opt. Exp.*, vol. 17, no. 19, pp. 16549–16557, 2009.

[13] S. M. Sze, *Physics of Semiconductor Devices*. New York: Wiley, 1981 ch. 5.

[14] Y.-C. Wang, "Small-signal characteristics of a Read diode under conditions of field-dependent velocity and finite reverse saturation current," *Solid State Electron.*, vol. 21, no. 4, pp. 609–615, 1978.

[15] T. Misawa, "Multiple uniform layer approximation in analysis of negative resistance in p-n junction in breakdown," *IEEE Trans. Electron Devices*, vol. 14, no. 12, pp. 795–808, Dec. 1967.

[16] F. K. Manasse and J. S. Shapiro, "An improved dispersion relationship for the P-N junction avalanche diode," *IEEE Trans. Electron Devices*, vol. 15, no. 5, pp. 282–289, May 1968.

[17] J. R. Grierson and S. O'Hara, "A comparison of silicon and gallium arsenide large signal IMPATT diode behavior between 10 and 100 GHz," *Solid-State Electron.*, vol. 16, pp. 719–741, 1973.

Daoxin Dai (M'07) received the B. Eng. degree from the Department of Optical Engineering, Zhejiang University, Hangzhou, China, and the Ph.D. degree from the Royal Institute of Technology (KTH), Stockholm, Sweden, in 2000 and 2005, respectively.

He joined Zhejiang University as an Assistant Professor and became Associate Professor in 2007. He is currently a Visiting Scholar in the Department of Electrical and Computer Engineering, University of California, Santa Barbara. His research interests include silicon microphotonic/nanophotonic integrated devices. He has authored and coauthored more than 50 refereed international journals papers.

Dr. Dai is a member of Optical Society of America and International Society for Optical Engineers.

Mark J. W. Rodwell (F'03) received the B.S. degree from the University of Tennessee, Knoxville, in 1980, and the M.S. and Ph.D. degrees from Stanford University, Stanford, CA, in 1982 and 1988, respectively.

From 1982 to 1984, he was with AT&T Bell Laboratories, Whippany, NJ. He is currently a Professor and Director of the University of California at Santa Barbara (UCSB) Nanofabrication Laboratory and the National Science Foundation Nanofabrication Infrastructure Network at the Department of Electrical and Computer Engineering, UCSB, Santa Barbara. His research interests include high-bandwidth InP bipolar transistors, compound semiconductor field-effect transistors for very large scale integration (VLSI) applications, and millimeter-wave integrated circuit design in both silicon VLSI and III–V processes.

Dr. Rodwell was the recipient of the 1989 National Science Foundation Presidential Young Investigator Award for his work on GaAs Schottky-diode ICs for subpicosecond/millimeter-wave instrumentation. He was also awarded the 1997 IEEE Microwave Prize.

John E. Bowers (F'93) received the M.S. and Ph.D. degrees from Stanford University, Stanford, CA.

He is currently the Director of the Energy Efficiency Institute and a Professor in the Department of Electrical and Computer Engineering, University of California, Santa Barbara (UCSB). He is also CTO and cofounder of Calient Networks and Chairman of the Board of BioIQ, Santa Barbara, California. He is the cofounder of the Center for Entrepreneurship and Engineering Management, and founder of Terabit Technology (sold to Ciena). He was also with AT&T Bell Laboratories and Honeywell before joining UCSB. His research interests include silicon photonics, optoelectronic devices, optical switching, and transparent optical networks. He is the author or coauthor of eight book chapters, 450 journal papers, 700 conference papers, and holds 52 patents.

Dr. Bowers is a fellow of the Optical Society of America (OSA) and the American Physical Society, and a recipient of the IEEE Laser and Electro-Optics Society (IEEE LEOS) William Streifer Award and the South Coast Business and Technology Entrepreneur of the Year Award. He was an elected member of the IEEE LEOS Board of Governors, a LEOS Distinguished Lecturer, and Vice President for Conferences for LEOS. He is a member of the National Academy of Engineering. He and coworkers received the ACE Award for Most Promising Technology for the hybrid silicon laser in 2007.

Yimin Kang (M'06) received the B.S. degree from Tsinghua University, Beijing, China, and the M.S. and Ph.D. degrees in material science and engineering from University of California, San Diego, in 1999 and 2003, respectively.

She is currently a Senior Researcher of Intel Corporation, Santa Clara, CA, since 2006. Before joining Intel, she was a Post Graduate Researcher in the University of California, where she was engaged in the development of single photon detector for 1.3–1.55 um wavelength. Her research interests include silicon photonics and high performance avalanche photodiodes.

Dr. Kang is a member of Laser and Electro-Optics Society.

Mike Morse (M'01) received the B.S. degree in ceramic engineering from Ohio State University, Columbus and the Ph.D. degree in materials science and engineering from Massachusetts Institute of Technology, Cambridge, in 1997. His Ph.D. thesis was on the erbium doping of epitaxial SiGe for light emission.

He is currently a Principal Engineer in the Photonics Technology Laboratory at Intel Corporation, Santa Clara, CA, where he has been engaged in the research on SiGe p-i-ns and avalanche photodetectors.